Cell Reports
Physical Science

CellPress
OPEN ACCESS

Article

Edge-enhanced ultrafast water evaporation from graphene nanopores

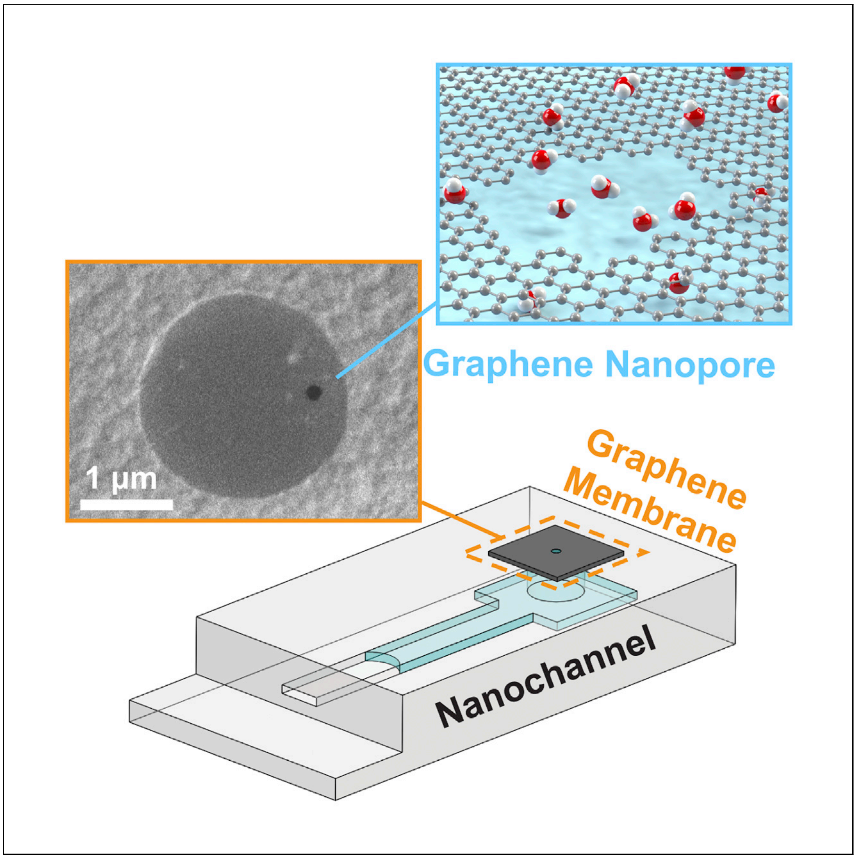

Siyang Xiao, Kaixin Meng, Quan Xie, Linxin Zhai, Zhiping Xu, Hao Wang, Chuanhua Duan

duan@bu.edu

Highlights

3D hybrid silica nanochannel graphene nanopore devices are designed and fabricated

Kinetically limited water evaporation is measured from graphene nanopores

The evaporation flux increases as the graphene nanopore diameter decreases

Edge-enhanced ultrafast water evaporation is observed at different temperatures

Graphene nanoporous membranes can be used as the ultimate ultrathin nanoporous membrane evaporators. To better understand and develop such membrane evaporators, Xiao et al. experimentally study kinetically limited water evaporation from single and multiple graphene nanopores with various diameters by using 3D hybrid nanofluidic devices and discover edge-enhanced ultrafast water evaporation.

Xiao et al., Cell Reports Physical Science 3, 100900
June 15, 2022 © 2022 The Author(s).
https://doi.org/10.1016/j.xcrp.2022.100900

Cell Reports
Physical Science

CellPress
OPEN ACCESS

Article

Edge-enhanced ultrafast water evaporation from graphene nanopores

Siyang Xiao,[1] Kaixin Meng,[2] Quan Xie,[1] Linxin Zhai,[3] Zhiping Xu,[3] Hao Wang,[2] and Chuanhua Duan[1,4,5,*]

SUMMARY

Graphene nanoporous membranes are the ultimate ultrathin nanoporous membranes and have enormous potential applications due to efficient heat and mass transfer that is limited only by interfacial evaporation kinetics. Developing such membranes requires fundamental understanding of evaporation at the single-pore level, which has remained largely unexplored. Herein, we report the experimental study of kinetically limited evaporation from single/multiple circular graphene nanopores with diameters from 24 to 347 nm. We show that, despite a wide variation, the evaporation flux increases as nanopore diameter decreases and that the maximum evaporation flux exceeds the upper kinetic limit predicted by the classical Hertz-Knudsen relation for nanopores with diameters below 60 nm. We associate the enhancement with edge-facilitated evaporation and minimum contaminant accumulation at the liquid-vapor interface. We further find that such enhanced ultrafast evaporation exhibits a temperature-insensitive but diameter-dependent manner. Our work provides new insights into nanoscale evaporation and will shed light on developing 2D nanomaterials-based membrane evaporators.

INTRODUCTION

Ultrathin nanoporous membrane evaporators with thickness below 1 μm have attracted wide attention over the last decade due to their promising applications in a variety of evaporation-involved applications, including thermal management,[1–3] membrane distillation,[4] steam generation and salt harvesting,[5] liquid atomization,[6] and water desalination.[7] The nanoscale pores in such evaporators ensure large capillary force for liquid refilling and small thermal resistance for efficient heat transfer between the solid membrane and the liquid-vapor interface.[8–10] Meanwhile, the ultrathin thickness of these evaporators reduces hydraulic resistance for liquid transport toward the interface and possible contaminant accumulation.[11] Benefiting from these advantages, ultrathin nanoporous evaporators exhibit significantly enhanced evaporation performance compared with other types of evaporators. It has been shown that evaporation from such membranes can even reach the kinetic limits predicted by the classical Hertz-Knudsen (H-K) equation, which is traditionally considered the ultimate performance of membrane evaporators.[12]

Can we further improve the performance of ultrathin nanoporous membranes? One way to do so is to minimize the thickness of the ultrathin nanoporous membranes to completely diminish the contaminant accumulation and transport resistance associated with liquid refilling.[11] This can be achieved by using 2D materials with atomic thickness, and graphene will be the best candidate because of its excellent mechanical property.[13,14] Another way is to exploit other mechanisms that can boost

---

[1] Department of Mechanical Engineering, Boston University, Boston, MA 02215, USA

[2] Department of Energy and Resources Engineering, Peking University, Beijing 10084, China

[3] Applied Mechanics Laboratory, Department of Engineering Mechanics, and Center for Nano and Micro Mechanics, Tsinghua University, Beijing 10084, China

[4] Division of Materials Science and Engineering, Boston University, Boston, MA 02215, USA

[5] Lead contact

*Correspondence: duan@bu.edu

https://doi.org/10.1016/j.xcrp.2022.100900

evaporation beyond classical evaporation from the liquid-vapor interface. Edge-facilitated evaporation, which continuously enhances evaporation because of special liquid-solid interactions at the pore edge, is such a mechanism.[12,15,16] Coincidentally, a recent simulation study showed that the edge of graphene nanopores would lead to such enhanced evaporation.[15] Since graphene nanoporous membranes can simultaneously harness these two approaches to further enhance evaporation, it is possible to use them to develop the best and ultimate ultrathin nanoporous membranes, achieving performance beyond the classical limit while being mechanically stable.

Despite the great promise, there are several challenges in developing and optimizing graphene nanoporous membrane evaporators. On the one hand, mature and facile methods are needed to produce scalable graphene porous graphene membranes with high graphene quality, well-controlled pore size, and pore density.[17] Current methods such as ozone treatment,[18,19] oxygen plasma,[20,21] and focused ion beam drilling[14,22] either do not have good control of pore size and density or only can be used at a small scale for proof of concept. On the other hand, fundamental knowledge of evaporation at the single graphene pore level is still missing. In fact, there have been no systematic experimental studies of evaporation from graphene nanopores, and the effects of nanopore diameter, pore density, and operating conditions on evaporation flux remain largely elusive.

In this work, we focus on tackling the second challenge in developing/optimizing graphene nanoporous membrane evaporators and experimentally measuring the kinetically limited evaporation from graphene nanopores. We studied the dependence of evaporation flux on pore diameter, pore density, and operating temperature and quantified the contributions from graphene pore edge and the rest of the meniscus on ultrafast evaporation of graphene nanopores.

RESULTS AND DISCUSSION

Hybrid nanochannel-nanopore conduits for evaporation measurements

We invented a hybrid nanochannel-nanopore conduit design to accurately measure the evaporation rate from single graphene nanopores. In this device design, graphene nanopores were connected to a transparent silica nanochannel with a channel height larger than the nanopore radius (as the schematic shown in Figure 1A; the device dimensions can be found in Note S1). When evaporation starts in a water-filled nanochannel-nanopore conduit, two menisci will be formed at the graphene nanopore and inside the silica nanochannel, respectively. Because the confinement difference results in a capillary pressure difference, the meniscus at the graphene nanopore will be pinned, and the meniscus in the silica nanochannel will continuously recede. Consequently, the evaporation rate from the meniscus at the graphene nanopore can be measured by tracing the meniscus receding of the nanochannel after quantifying contributions due to drying along the nanochannel (see Note S2).[23] We have used a similar device design to study ultrafast diameter-dependent evaporation from silicon nitride nanopores with great success.[12]

The hybrid silica nanochannel-graphene nanopore devices were fabricated by wet transferring graphene over an opened micropore reservoir at the end of a silica nanochannel made of a sacrificial-layer-etching method (detailed fabrication procedure and geometric characterization can be found in Note S1). The resulting suspended graphene membrane has a typical size of 2–5 μm in diameter (Figure 1B). A He or Ga focused ion beam was used to drill nanopores on the suspended membrane, generating graphene nanoporous membranes with pore numbers ranging

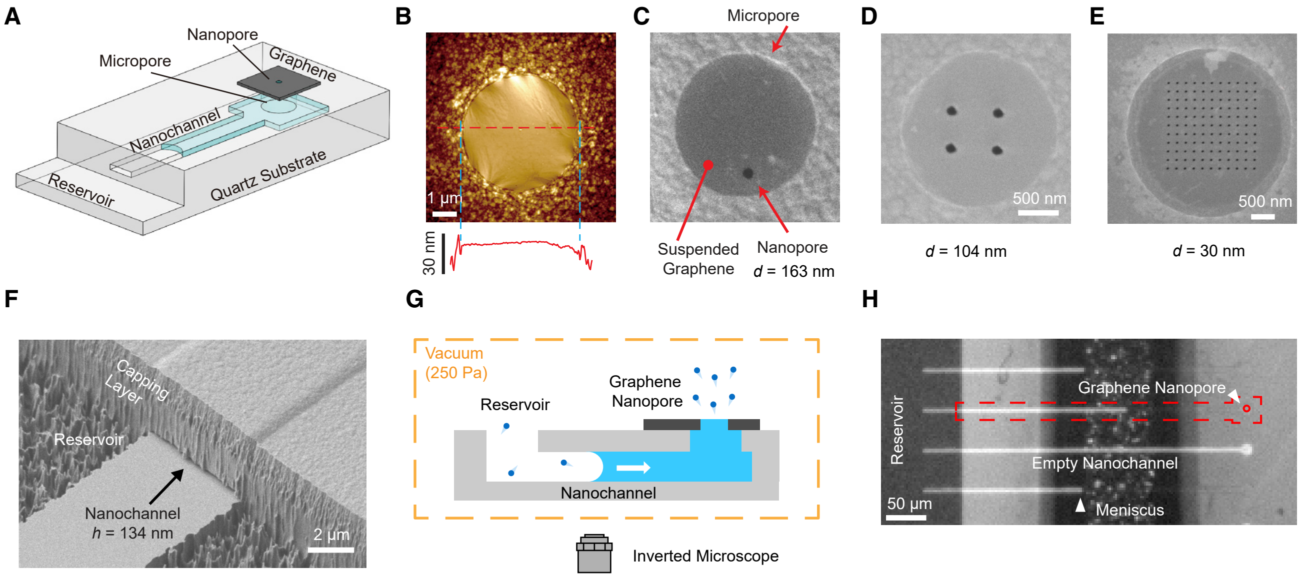

Figure 1. Hybrid nanochannel-nanopore conduits for graphene nanopore evaporation measurments

(A) Schematic of hybrid silicananochannel-graphene nanopore conduit.

(B) Scanning image from AFM of a nanopore-free graphene membrane. The suspended graphene over the micropore area shows notably lower roughness than graphene conformally transferred over the rough silicon oxide surface.

(C–E) SEM images of drilled nanopores on suspended graphene membranes, with varied pore diameter and quantity, forming single nanopores (C), small array of nanopores (E), and large array of nanopores (E).

(F) SEM image captured from the reservoir showing the slit nanochannel ($h = 143$ nm) embedded in the quartz substrate. The smooth surface in the bottom left corner is the extending floor of the nanochannel.

(G and H) Schematic of the evaporation experiment set-up and the captured optical image. The fabricated device is enclosed in a vacuum chamber over an inverted microscope, which captures the movement of the meniscus, as shown in (H).

from one to a few hundred, and pore diameters ranging from 20 to 340 nm (Figures 1C–1E). The 2D silica nanochannel, with a typical width and height of 5 μm and 100–300 nm, respectively, was embedded 2.5 μm underneath the graphene membrane plane (Figure 1F).

The fabricated devices were carefully examined via scanning electron microscope (SEM) and optical microscope, after which an ethanol-filling process was conducted before water introduction and water evaporation experiments. Due to the low surface tension, ethanol was able to fully fill the hybrid nanochannel-nanopore device. We found that this process was critical, as direct water introduction would always leave bubbles in the micropore reservoir underneath the suspended graphene membrane, which caused the failure of the following evaporation experiment because the bubble would expand during water drying in the nanochannel. After ethanol filling, the device was placed in a deionized water bath to replace the ethanol inside the hybrid nanochannel-nanopore device with water. We then used clean wipes to remove the water on top of the graphene membrane and placed the device in a vacuum chamber ($P_{vac} = 250$ Pa) over an inverted microscope (Olympus IX81) to perform the evaporation experiments (Figure 1G). Under this vacuum condition, the evaporation from graphene nanopore(s) is not limited by vapor diffusion away from the evaporation interface(s), and the hybrid conduit design also ensures sufficient water supply toward the interface(s) (see Note S3). As a result, kinetically limited evaporation is achieved. To extract the evaporation rate/flux, we used a high-speed camera (Hamamatsu ORCA-Flash4.0) to record the meniscus receding in the silica nanochannel (see Figure 1H and Note S2).

Membrane integrity

The integrity and cleanliness of the graphene nanoporous membrane are extremely critical for accurate evaporation measurements. Although pristine graphene has been shown to be impermeable to all regular gas, liquid, and dissolved ions, damage on the graphene membrane may leak molecules, causing overestimation of the evaporation rates and fluxes from graphene nanopores.[17,18,24,25] On the other hand, contaminants from the ambient environment and ethanol/water solutions may block the nanopore, which reduces or diminishes the actual evaporation area and leads to underestimation of the evaporation flux. In this work, we performed multiple procedures to ensure membrane integrity and cleanliness, including inspecting the graphene membrane with SEM, examining the ethanol-filling process in the connected silica nanochannel, and checking the meniscus-receding process during the evaporation experiment.

The first method we used to check the integrity and cleanliness was from the SEM inspection. Before performing the evaporation experiment, we used SEM to carefully examine the nanoporous graphene membrane of each hybrid conduit and discarded those with visible defects, contaminant-blocked nanopore(s), folded graphene, and/or multilayer graphene. After the experiment, we inspected the graphene membrane again to confirm the membrane quality. The device is considered good only when both pre- and post-experiment SEM scans show clear nanopore(s) present on a defects-free graphene membrane, which, in principle, should ensure the openness of nanopores during the experiments (see examples in Note S4).

The second method we used to check the quality of the nanoporous graphene membrane was ethanol filling in the silica nanochannel. For silica nanochannels whose micropores are covered with suspended graphene membranes without drilled holes and visible defects (which means defects are smaller than 5 nm), we found that ethanol filling was quick at the beginning and then became very slow (see Figure 2A). This is expected, as the trapped gas in the nanochannels cannot escape and will only gradually dissolve in ethanol. The movement of the meniscus in such nanochannels exactly follows the model reported by Phan et al., which accounts for both the capillary filling and air pocket shrinking[26] and also perfectly matches ethanol filling in close-end silica nanochannels (see Note S5). This confirms that pristine graphene is an impermeable membrane for air water vapor, and the contact between graphene and silica substrate does not contribute to leakage. In contrast, for hybrid silica nanochannels integrated with nanoporous graphene membranes (effective pore diameters above 20 nm), the ethanol filling was exactly the same as that in an open-end silica nanochannel (without any graphene membrane over the micropore) with the same geometry—the advancing meniscus quickly squeezed the air out of the nanochannel through the opening and filled the entirety of empty space. In this case, the meniscus prorogation followed the classic Washburn equation.[27] It is worth noting that we also observed that the ethanol filling in certain hybrid conduits was slower than that in the open-end nanochannels but faster than that in the closed-end silica nanochannels or pristine-graphene sealed nanochannels. In these cases, we believe the graphene nanopores were mostly blocked and only small openings (less than 20 nm) were left to form leakage (more discussions can be found in Note S5). As we could not measure the actual opening on these types of graphene membranes, we did not use them for the evaporation experiments.

The third measure, which also offered the best *in situ* evaluation of the quality of the graphene nanoporous membrane, was examining the meniscus receding in the

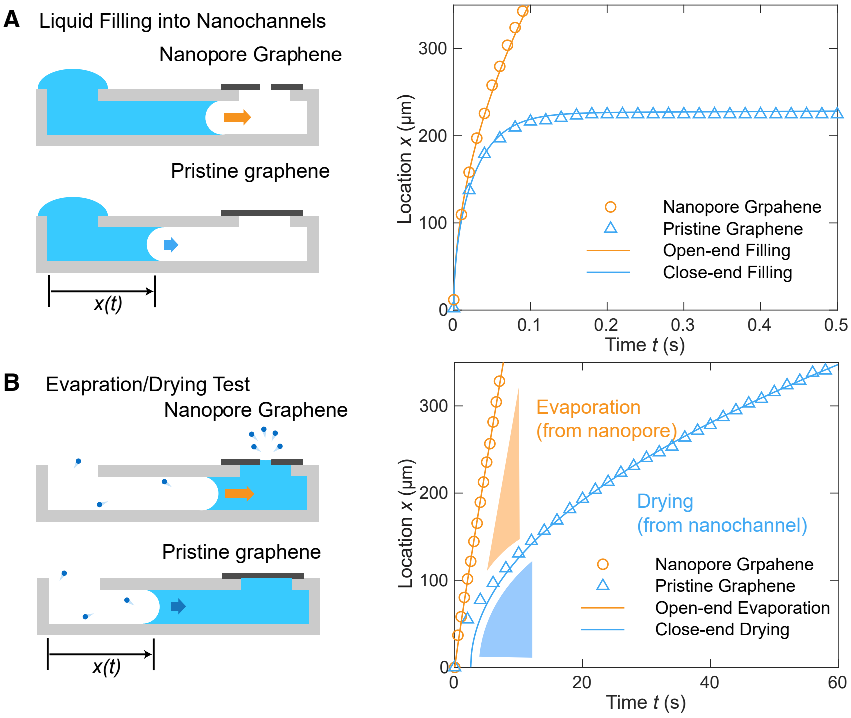

Figure 2. Meniscus movement tracking during filling and drying experiments

(A) Tracking of meniscus advancing during the filling test. The orange circles represent the observed meniscus positions in an open-end nanochannels (covered with nanopore graphene), and the blue triangles represent the observed meniscus positions in the closed-end nanochannel (covered with pristine graphene). The orange solid line plots the predicted tracking based on the Washburn equation; the blue solid line plots the predicted tracking based on the closed-end filling model.

(B) Tracking of meniscus receding during drying and nanopore evaporation test. The blue solid line represents the prediction of drying only in a closed-end nanochannel; the orange solid line represents the meniscus receding as a result of drying in the nanochannel and evaporation from the nanopore. The different area (denoted by the orange shade) between drying only (the blue line) and drying with nanopore evaporation curve (the orange line) represents the evaporation contribution from the nanopore.

connected silica nanochannel during the drying/evaporation experiment. We noticed that, for silica nanochannels connected with the pristine graphene membranes, meniscus receding slowed down with time and showed a perfect square root time dependence. This can be understood as the filled water being dried out only by unidirectionally leaving the channel through the reservoir, which resulted in a linearly increasing drying resistance as the meniscus receded. Fitting the meniscus receding curve with a parabolic function $x = \sqrt{u_{dry} t}$ (which is the solution of the differential equation $\frac{dx}{dt} = \frac{u_{dry}}{2x}$), we were able to find the drying constant u_{dry} of the silica nanochannel, which is majorly determined by the nanochannel geometry.[23,28] For comparison, we also recorded the meniscus receding in close-end silica nanochannels (micropore sealed with silica), which share the same geometry as the pristine graphene covered conduits. In both conduits, the menisci recede in the same behavior with identical u_{dry}, which further confirms the leak-free of prestine graphene membranes (more details in Note S2).

In contrast, for the hybrid silica-nanochannel graphene nanopore conduit, we found that the meniscus in the silica nanochannels receded faster than in the previous case

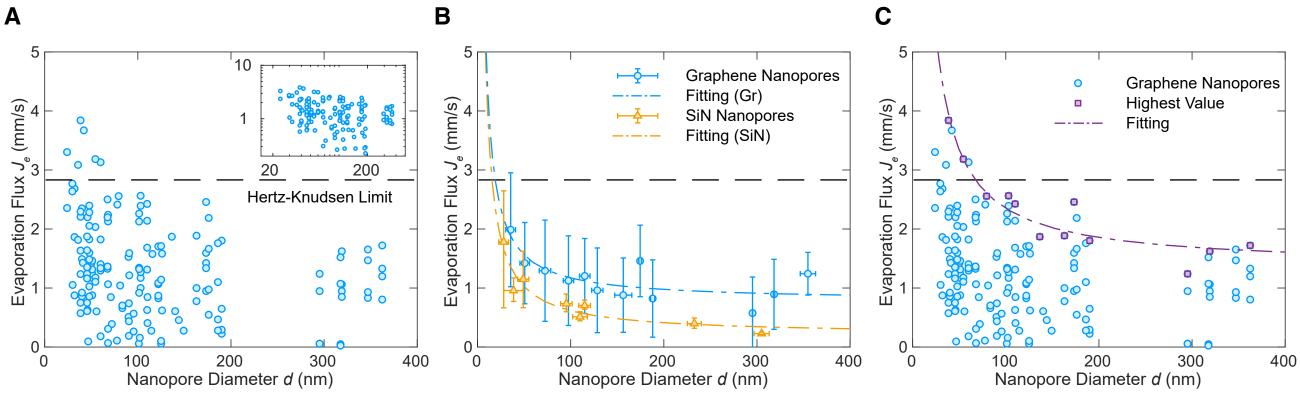

Figure 3. Kinetically limited evaporation flux from graphene nanopores

(A) Evaporation flux from graphene nanopores (normalized by nanopore area) versus nanopore diameter. The black dashed line represents the Hertz-Knudsen (H-K) limit ($\sigma_e = 1$). The inset shows the same plot in log scale.

(B) Graphene nanopore evaporation flux data in the plot (A) is averaged by each 20-nm nanopore diameter group. The yellow triangles represent kinetically limited evaporation flux measured from 280-nm-thick Si_3N_4 nanopores in previous work. The blue and yellow dashed lines represent fitting between evaporation flux and reciprocal of diameter. The error bars of graphene nanopore are defined as the SD of measured evaporation flux and nanopore diameter in each group.

(C) The purple squares mark the highest graphene nanopore evaporation flux of each diameter range as grouped in plot (B). The purple dashed line represents the fitting.

(Figure 2B) and that the meniscus position $x(t)$ can be well described by a different differential equation

$$\frac{dx}{dt} = \frac{u_{dry}}{2x} + V_r \qquad \text{(Equation 1)}$$

where V_r is the additional receding speed due to the evaporation, and $V_r = \frac{J_e N \pi d^2}{4wh\rho_l}$. J_e (mm/s) is the evaporation flux from the graphene nanopores, d is the nanopore diameter, N is the number of nanopores on the membrane, ρ_l is the density of liquid water, and w and h are the nanochannel width and height, respectively. This is because both the drying in the nanochannel and the evaporation from the graphene nanopore contribute to the meniscus receding. By fitting the meniscus-receding curve with the analytical solution of Equation 1, which is $t = \frac{x}{V_r} - \frac{u_{dry}}{2V_r^2}\ln\left[\frac{2V_r x}{u_{dry}} + 1\right]$, a constant evaporation flux J_e can be extracted (the derivation and the corresponding error analysis can be found in Note S2).

We found that if the nanopore is partially blocked during the evaporation, the meniscus receding curve can no longer be perfectly fitted by Equation 1, because the blockage would result in a change of evaporation area and, thus, a change of evaporation rate. We also found that if the graphene membrane is damaged during the vacuum evaporation process, the meniscus on the graphene membrane side would recede together with the meniscus on the silica nanochannel side.

Together with SEM examination, analysis of ethanol filling, and meniscus-receding recording during evaporation, we are able to tell if the graphene membrane is damaged or there are air bubbles remaining in the hybrid conduits during the evaporation experiment. Moreover, we can quickly identify those devices where nanopores are largely blocked before and during the evaporation experiments.

Diameter-dependent ultrafast evaporation flux

In Figure 3A, we plotted the measured evaporation flux normalized by graphene nanopore area as a function of the nanopore diameter when the experiment was performed under room temperature (22°C). For comparison, we also plotted the evaporation flux predicted by the classic H-K relation, which can be written as

$$J_e = \sqrt{\frac{M_w}{2\pi R_g}}\left[\sigma_e \frac{P_{eq}}{\sqrt{T_i^L}} - \sigma_c \frac{P^V}{\sqrt{T_i^V}}\right] \qquad \text{(Equation 2)}$$

where M_w is the molar weight of water, R_g is the universal gas constant, σ_e and σ_c are evaporation coefficient and condensation coefficient, respectively, T_i^L and T_i^V are liquid and vapor temperature at the interface, P_{eq} is water vapor pressure in equilibrium with water meniscus $P_{eq} \approx P_{sat}(T_i^L)$ for the investigated dimeter range, and P^V is the vapor phase pressure ($P^V = P_{vac}$). Since in the vacuum conditions P^V is negligible compared with P_{eq}, the above relation can be simplified as $J_e = \sigma_e \sqrt{\frac{M_w}{2\pi R_g T_i^L}} P_{sat}(T_i^L)$. J_e reaches the upper H-K limit (i.e., the sonic limit) J_{HK} when $\sigma_e = 1$.[29,30]

The first observation from Figure 3A is that, despite our extensive examination of the quality/cleanness of the graphene nanopore membranes, the evaporation fluxes from different graphene nanopores of the same size showed wide variation, and the smaller the nanopore the more significant the variation. We hypothesized that part of the variation could come from the measurement uncertainty, since inaccurate measurement of the pore diameter, the meniscus-receding speed, and nanochannel geometry can together cause up to 20% uncertainty for each data point (see error analysis in Note S2). We also hypothesized that partial nanopore blockage might attribute to the wide variation. Even though we used three methods to check the integrity and cleanness of the nanoporous graphene membranes, we still cannot tell whether the pores were just partially blocked during ethanol filling and water evaporation but became "clean" during post-evaporation SEM characterization. In fact, we found that in some cases (less than 10% of the results; see in Figure 3A), the evaporation fluxes were abnormally low or even almost zero compared with fluxes measured from similar-sized nanopores or other measurement results from the same nanopore but at different times.

Nevertheless, overall, the evaporation flux shows an increasing trend as the diameter decreases. Furthermore, as the diameter decreases to below 60 nm, a portion of the measured evaporation fluxes exceeds the sonic limit. Although ultrafast evaporation beyond the sonic limit has been reported before in silica nanoslits and silicon nitride nanopores, it was discovered that thin-film evaporation outside of the nanochannel/nanopore is the actual cause of those observation.[10,12] As we confirmed that there is no thin-film evaporation outside of the graphene nanopore (see Note S4), these ultrahigh evaporation fluxes from graphene nanopores thus become the first experimental evidence that evaporation from nanopores can exceed the classical limit.

To better understand the diameter dependence and the ultrafast evaporation flux, we grouped data from similar-sized (20 nm for each group) graphene nanopores and replotted the data in Figure 3B, where the value and error bar of each data point represent the averaged value and SD in each sized group, respectively. We also compared the evaporation flux from graphene nanopores with the kinetically limited evaporation flux from silicon nitride nanopores (pore thickness 280 nm; the surface is hydrophobic to remove thin-film evaporation out of the nanopore) from our previous work, which was measured under the same experimental conditions using similar methods.[12] It is clear that most of the graphene nanopores exhibited faster evaporation fluxes than the silicon nitride nanopores of the same diameter. This is very interesting, as evaporation from these two types of nanopores should be limited only by the evaporation kinetics and not the liquid/vapor transport.

The higher evaporation flux of the graphene nanopores compared with the silicon nitride nanopores and its diameter dependence can possibly be explained by two edge effects. The first one stems from the unique interaction between graphene edge and water molecules. Graphene is known to be atomically smooth and hydrophobic.[31] In the molecular view, lacking hydrogen bonds, the graphene surface repels water molecules, which has been reported extensively for liquid water and ion transport on/across graphene.[32,33] Therefore, water molecules at the graphene edge can become more "activated" and are likely to escape the hydrogen bonds network with other water molecules and thus evaporate more easily. This effect has been confirmed by a recent MD simulation study done by Feng and Xu, who showed that water at the edge region of graphene nanopore has higher potential energy than in bulk phase, and water tends to travel to the edge region for evaporation.[15] As a result, the higher evaporation flux at the edge of the graphene nanopore elevates the overall evaporation rate and even exceeds the H-K limit. Since smaller nanopores have higher perimeter-to-area ratios, such edge-facilitated evaporation will become more prominent in smaller nanopores, which leads to a diameter dependence.

The second edge effect results from the surface charge of the graphene nanopore. It is well known that graphene nanopore is negatively charged in deionized water due to its broken carbon-carbon bonds at the edge and being terminated by oxygen-functionalized groups.[34–38] The negative surface charges can repel co-ions (i.e. hydroxide ions) and attract the positively charged hydronium ions inside the nanopores, forming electrical double layers.[39] Within the electrical double layers, an increase of local concentration of hydronium ions is expected, and the presence of extra hydronium ions can also affect local hydrogen bonds and water structure, increasing the overall water evaporation coefficient and evaporation flux.[40] For nanopores with diameter comparable to the thickness of the electrical double layers, since the hydronium ion concentration is inversely proportional to the nanopore diameter, smaller pores would also be affected more.[12,41,42]

It is worth noting that both effects are very sensitive to the edge composition and structure,[15] which has also been found to significantly affect water and ion transport across the graphene nanopores.[20,38] As graphene is only one atom thick and the edge of graphene nanopores includes only a few hundred atoms, slight changes in functional groups, defects, and structures between different nanopores would lead to different edge effects and, thus, different evaporation behavior. This can thus also explain why there is a large variation of evaporation flux for similar-sized graphene nanopores, especially those with smaller diameters.

To further understand how the edge affects affect kinetically limited evaporation, we fitted experimental results of the graphene and silicon nitride nanopores with the following function, $J_e = \frac{(A\pi d^2 + \pi dB)}{\pi d^2} = A + \frac{B}{d}$, which represents the linear relationship between the evaporation flux and the reciprocal of the nanopore diameter (see the blue and yellow dashed lines in Figure 3B). In this formula, A represents the evaporation flux from the central region of the meniscus, and B/d is the contribution from the edge, which may be related to the edge-facilitated evaporation or the surface charge effect. Our results show $A_G = 0.78$ mm/s and

$B_G = 38.88\ \text{nm}\cdot\text{mm/s}$ ($R^2 = 0.64$) for graphene nanopores and $A_S = 0.21\ \text{mm/s}$ and $B_S = 40.74\ \text{nm}\cdot\text{mm/s}$ ($R^2 = 0.90$) for silicon nitride nanopores.

There are several interesting facts from these fitting results. First, the edge effects clearly play an important role in the kinetically limited evaporation flux for both graphene and silicon nitride nanopores. In both types of ultrathin nanopores, the edge contribution actually becomes dominant when the nanopore's diameter is below 100 nm.

Second, graphene nanopores and silicon nitride nanopores share close value of edge contribution (B). This is possibly because the experimental data may include a variety of graphene pore conditions (e.g., different edges and/or blockage conditions). To further explore the upper limit of the edge effects, we marked the highest measured evaporation flux for each group of the graphene nanopore evaporation data in Figure 3C, and acquired a fitting of $J_e = A'_G + \frac{B'_G}{d} = 1.19\frac{\text{mm}}{\text{s}} + \frac{98.95}{d}\ \frac{\text{nm}\cdot\text{mm}}{\text{s}}$ ($R^2 = 0.89$). These data and the fitting curve to some extent represent graphene nanopores with the most favorable edge conditions and/or the least blockage states for evaporation. B'_G of these graphene nanopores is significantly higher than B_S, possibly because such graphene nanopores could benefit from both effects, whereas silicon nitride nanopores would not benefit from the first one due to their hydrophilic nature. It is also worth noting that the evaporation flux of such ideal graphene nanopores becomes higher than the H-K limit when the nanopore diameter is below 70 nm. Although due to technical issues we currently cannot identify what the ideal edge structures are and are also not able to dissect the separate contributions from these two edge effects, these data and fitting further confirm that graphene nanopores hold great promise to build the ultimate ultrathin nanoporous evaporators with performance beyond the sonic limit.

Last but not the least, the bulk contribution in the graphene nanopores $A_G = 0.78\ \text{mm/s}$ and $A'_G = 1.19\ \text{mm/s}$ are also significantly larger than that in silicon nitride nanopores $A_S = 0.21\ \text{mm/s}$. This difference cannot be explained by any edge effects. Also, it cannot be explained by the liquid/vapor transport limit, as these two limits are significantly larger than the kinetic limit and evaporation should thus be kinetically limited only.

We hypothesize that this difference of bulk evaporation contribution may result from minimized contaminant accumulation in graphene nanopores. It is well known that contaminants in water can significantly affect the water evaporation coefficient and therefore the water evaporation flux.[30,40,43] At steady-state, since the contaminant accumulation at the nanopore liquid-vapor interface caused by convective flux $[uc(x)]$ should counterbalance the diffusion flux toward the bulk liquid $\left[-D_c\frac{dc(x)}{dx}\right]$, the local concentration of the contaminants at the interface c_i can therefore be written as[11]

$$c_i = c_b \exp\left(\frac{ul}{D_c}\right) \qquad \text{(Equation 3)}$$

where c_b is the concentration of such contaminants in the bulk liquid, l is the thickness of the nanopore, u is the liquid flow velocity induced by nanopore evaporation, and D_c is the diffusion coefficient of the contaminants in water. For ultrathin nanopores, the exponential term is small, and a linear correlation between c_i and the nanopore thickness $c_i = c_b\left(1 + \frac{ul}{D_c}\right)$ is thus expected. Because graphene is only one atom thick, but silicon nitride is a few hundred nanometers in thickness, the contaminant accumulation in these two types of ultrathin nanopores will be significantly different. It is expected that there is essentially no (or minimum) contaminant accumulation in the graphene nanopores but finite and non-negligible accumulation in silicon nitride nanopores, which possibly leads to the observed bulk concentration difference.

Another possible explanation is the difference between local heat transfer and the resulting local temperature change across the liquid-vapor interface. Although we usually consider evaporation from single or a small array of nanopores as an isothermal process, heat is still required to transfer from the solid substrate to the liquid-vapor interface during evaporation. Ghasemi and Ward[44] have demonstrated that such a heat transfer has a directional preference and that the interactions between water and the substrate play an important role. Meanwhile, Persad and Ward have also shown that, according to the statistical rate theory, the kinetically limited evaporation is extremely sensitive to the local temperature change across the liquid-vapor interface.[30] Because of the structure and property difference between graphene nanopores and silicon nitride nanopores, it is possible that graphene nanopores and silicon nitride nanopores have different heat transfer mechanisms to the liquid-vapor interface.

These are a few possible hypotheses, and there could be others as well. At this point, we still do not understand what causes the different "bulk" contributions in graphene and silicon nitride nanopores. Nevertheless, the advantage of graphene nanopores compared with ultrathin silicon nitride nanopores is very clear.

Evaporation performance under different conditions

To provide a more realistic guideline for future applications using large nanoporous graphene membranes, it is crucial to evaluate whether the observed ultrahigh evaporation performance and the diameter dependence are valid for graphene nanopores under different conditions.

We first check whether the pore numbers and porosity would affect the observed evaporation performance. Although the kinetically limited evaporation from graphene nanopores can approach or exceed the H-K limit, the evaporation rate is only on the order of $\sim 10^{-14}$ kg/s for a single nanopore. Therefore, the number of graphene nanopores and thus the membrane porosity need to be increased dramatically for any realistic applications. However, as the pore number and porosity increase, it is unclear whether the nanoporous graphene membranes can remain stable while allowing high evaporation rates and whether the increasing porosity would affect the observed high evaporation flux from individual nanopores.

To provide more insights on these questions, we separate the nanopore evaporation data presented in Figure 3 into three groups based on the number of nanopores on the graphene membrane as single nanopore ($N = 1$), small arrays ($1 < N < 10$), and large arrays of nanopores ($N \geq 10$, the highest N is 121). The equivalent porosity φ, for these nanopore arrays, varies between 0.1% and 10%. We replotted the evaporation flux separately in Figure 4, in which the blue dashed lines represent the same diameter dependence as shown in Figure 3B. We found that there is still a large variation in evaporation flux from similar diameters regardless the number of nanopores on one membrane. Nevertheless, the aforementioned diameter dependence can still be used to capture the change of evaporation flux for each of these three groups, which suggests that the observed diameter dependence is independent of graphene pore number and porosity, at least in the range we investigated. Moreover, the nanoporous graphene membranes remained intact after the intense evaporation experiments under vacuum, which demonstrates the feasibility of developing large graphene nanoporous evaporators. Combining these two observations, we can conclude that it is feasible to create large graphene nanoporous evaporators and

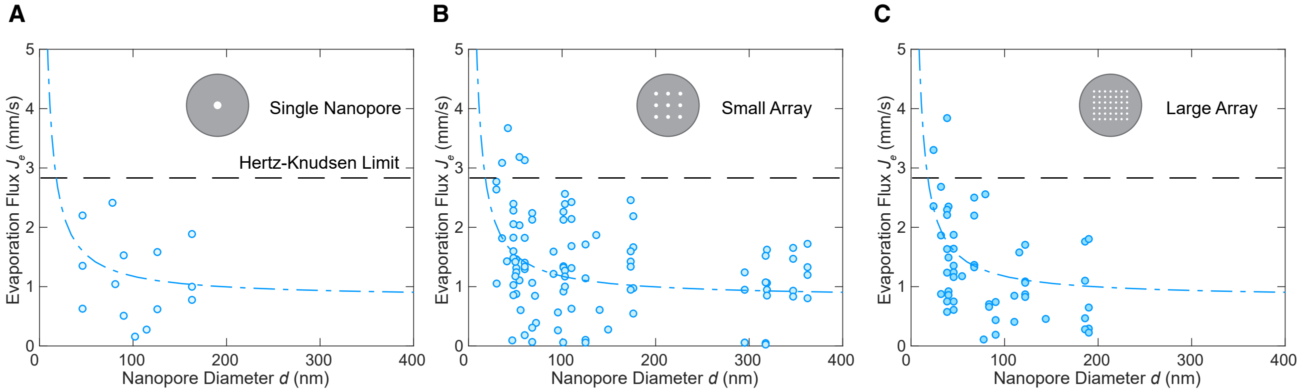

Figure 4. Effect of pore number and porosity on the evaporation flux

(A–C) Diameter-dependent evaporation flux for (A) single nanopores ($N = 1$), (B) the small array of nanopores ($1 < N < 10$), and (C) the large array of nanopores ($10 \leq N \leq 121$). The black dashed line represents the H-K limit; the blue dashed line represents the same diameter dependence fit from all data points regardless of nanopore number.

for a given porosity, the optimal strategy for achieving high evaporation performance is to fabricate relatively small nanopores instead of large ones.

Temperature is another important factor that affects the evaporation flux and is also the key operating parameter in applications such as membrane evaporators. We performed the nanopore evaporation experiments under different operating temperature (controlled by chip heater) and show the results in Figure 5A (details of experiment set-up can be found in Note S1). It is obvious that higher evaporation flux is measured at higher temperature. For example, for nanopores with a diameter of 34 ± 10 nm, the evaporation flux at 50°C is almost 10 times that at 22°C. However, the diameter dependence is still observed regardless of different temperature.

To further explore the temperature dependence, we compared the measured evaporation fluxes with the evaporation flux predicted by the H-K limit (assuming $\sigma_e = 1$, plotted as the black dashed line) in Figure 5B. Since P_{sat} is also determined by the temperature, the H-K limit becomes a sole function of the operating temperature, which increases almost exponentially as the temperature increases. Interestingly, we found that for the same-sized nanopores the measured evaporation flux from graphene nanopores followed the same trend as the H-K limit, but with different magnitude. The temperature dependence depicted by the H-K relation is therefore still valid for nanopore evaporation.

The strong diameter dependence of the evaporation flux, along with the validity of the H-K relation, indicates that the evaporation coefficient of graphene nanopores would not change with temperature but strongly depends only on the pore diameter. To confirm this, we normalized the evaporation flux based on the H-K limit at different temperature to obtain the evaporation coefficient σ_e $\left[\sigma_e = \frac{J_e}{J_e(\sigma_e = 1)}\right]$ and show its dependence on nanopore diameter in Figure 5C. Indeed, the $\sigma_e = a_G + \frac{b_G}{d}$ relation found at 22°C (blue dashed lines $a_G = 0.27$ and $b_G = 13.73$ nm) can be used to predict the trend in all other temperature conditions, indicating that the evaporation coefficient of graphene nanopore has no temperature dependence. This finding is consistent with a recent study of kinetically limited evaporation from ultrathin silicon nitride nanoporous membranes, where predication based on the H-K equation and a constant evaporation coefficient could well match experimental results over a large temperature

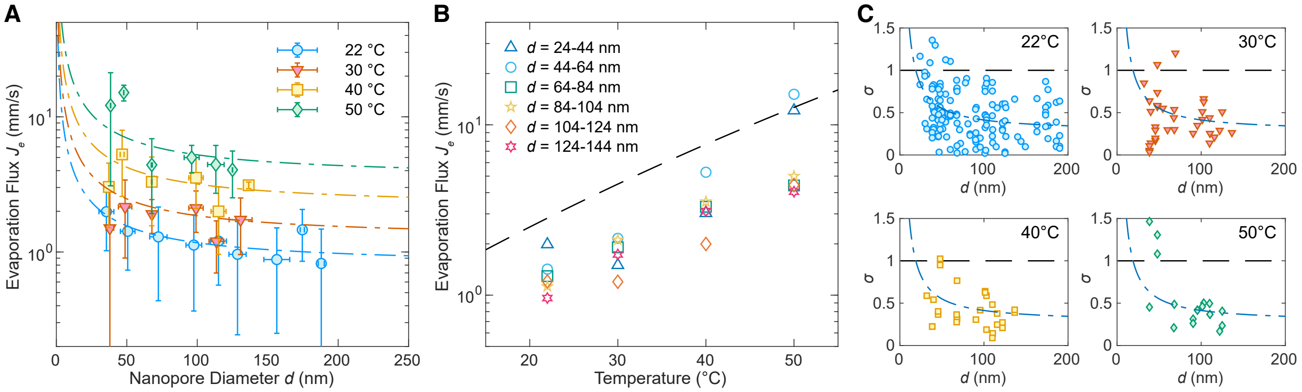

Figure 5. Effect of operating temperature on the evaporation flux

(A) Evaporation flux as a function of pore diameter at different temperatures. The evaporation flux always increases as the nanopore diameter decreases. Error bars represent SD of a group of data within corresponding diameter range (±10 nm). Dash-dot lines represent the same fitting when normalizing the evaporation flux to the H-K limit.

(B) Evaporation flux as a function of operating temperature. The black dashed line marks the H-K limit, which increases nearly exponentially with temperature. At each temperature condition, the smaller nanopore groups hold relatively higher evaporation flux compared with larger nanopore groups. The error bars (same as in A) have been hidden to better show all markers.

(C) Evaporation coefficient σ_e (normalized evaporation flux based on the H-K limit) as a function of nanopore diameter. Each point represents the result from one graphene membrane. In all subplots, the blue dashed lines represent the same fitting ($\sigma_e = a_G + \frac{b_G}{d}$) obtained from data at 22°C.

range.[45] However, the evaporation coefficient was estimated as 0.35 for their 200-nm silicon-nitride nanopores, while in graphene nanopores, we showed that it could have values larger than 1 due to the edge-facilitated evaporation and minimum contaminant accumulation, which further confirms the advantage of graphene nanoporous membrane evaporators.

In summary, we integrated monolayer graphene membranes into nanofluidic devices to investigate the water evaporation kinetics from the graphene nanopores. We used multiple procedures to secure the membrane integrity, thus ensuring that the device was capable of providing accurate evaporation flux measurement with the resolution down to single nanopore. The kinetically limited evaporation flux was found to be a reciprocal function of the nanopore diameter, where the smaller the nanopore, the higher the evaporation flux. At diameters below 100 nm, we even measured flux exceeding the sonic limit predicted by the classic H-K relation. The edge of the graphene nanopore is believed to play an important role to elevate the evaporation flux, and different functional groups of nanopore edge are hypothesized to be responsible for the variation in evaporation flux. The diameter dependence was also found to be insensitive to the number of nanopores and the operating temperature. These findings provide fundamental understanding of the evaporation kinetics in graphene nanoporous membranes and promising outlooks for various applications requiring high-performance evaporation.

EXPERIMENTAL PROCEDURES

Resource availability

Lead contact

Further information and requests for resources should be directed to and will be fulfilled by the Lead Contact, Chuanhua Duan (duan@bu.edu).

Materials availability

This study did not generate new unique reagents or materials.

Data and code availability

Raw data are available from the lead contact upon reasonable request.

Device fabrication

We first used photolithography and lift-off techniques to define a thin sacrificial layer of Cr with nanochannel pattern on a quartz substrate. Then, we used plasma-enhanced chemical vapor deposition (PECVD, SiH_4, and N_2O) to conformally deposit a 2.5-μm-thick amorphous SiO_2 capping layer over the Cr sacrificial layer. On top of the SiO_2 capping layer, another layer of Cr film was deposited and defined using lift-off techniques to expose the area of open reservoir and micropore. This second layer of Cr served as the hard mask for reactive ion etching (RIE) to etch through the SiO_2 capping layer and expose the nanochannel entrance at the open reservoir and first sacrificial layer of Cr at the micropore. Following this step, both the hard mask and the sacrificial layer were etched and released by Cr etchant to form the empty nanochannel. After the fabricated substrates were cleaned, graphene was wet-transferred onto the nanochannel chip. To be more specific, top-side graphene on the as-purchased graphene on copper foil (GrollTex, Inc.) was first spin-coated with poly(methyl methacrylate) (PMMA). After the back-side graphene was removed by oxygen plasma etching, the PMMA-graphene-Cu stack was floated in Cu etchant (Sigma-Aldrich) to remove Cu. Then the nanochannel chip was used to scoop out the PMMA-graphene stack and dry it. The PMMA was removed by acetone, followed by CO_2 critical-point drying, and H_2/Ar annealing at 340°C. Once the presence of suspended graphene over the micropore was confirmed by SEM, we used a focused ion beam (Ga ion for larger nanopore and He ion for smaller nanopore) to drill a nanopore on the graphene. Finally, we bonded the nanochannel chip with a silicon chip, which was etched through with two open windows for separate access of micropore and reservoirs. To perform the bonding, we stamped a thin layer of poly(dimethylsiloxane) (PDMS) using the silicon chip, aligned it with the nanochannel chip, and then cured the PDMS on a hotplate.

SUPPLEMENTAL INFORMATION

Supplemental information can be found online at https://doi.org/10.1016/j.xcrp.2022.100900.

ACKNOWLEDGMENTS

This work was supported by National Science Foundation (CBET-1653767 and CBET-1805421) and National Natural Science Foundation of China (No. 51976001). S.X., Q.X., and C.D. would like to thank the Photonics Center at Boston University for the use of their fabrication and characterization facilities. S. X. and C.D. are also grateful for the discussion with Matthias Kuehne, Samuel Faucher, Michael Strano, and Aaron Persad from MIT regarding possible explanations for enhanced kinetically limited evaporation fluxes from graphene nanopores.

AUTHOR CONTRIBUTIONS

C.D. conceived the idea and directed the project; S.X., Q.X., and C.D. designed the experiments; S.X., K.M., and Q.X. fabricated the samples and conducted the experiments; S.X., L.Z., Z.X., H.W., and C.D. analyzed the experimental data; and S.X. and C.D. wrote the initial draft. All authors participated in completing the final manuscript.

DECLARATION OF INTERESTS

The authors declare no competing interests.

Received: February 10, 2022
Revised: March 28, 2022
Accepted: April 20, 2022
Published: June 15, 2022

REFERENCES

1. Plawsky, J.L., Fedorov, A.G., Garimella, S.V., Ma, H.B., Maroo, S.C., Chen, L., and Nam, Y. (2014). Nano- and microstructures for thin-film evaporation—a review. Nanoscale Microscale Thermophys. Eng. *18*, 251–269. https://doi.org/10.1080/15567265.2013.878419.
2. Dai, X., Yang, F., Yang, R., Lee, Y.-C., and Li, C. (2013). Micromembrane-enhanced capillary evaporation. Int. J. Heat Mass. Transf. *64*, 1101–1108. https://doi.org/10.1016/j.ijheatmasstransfer.2013.05.030.
3. Hanks, D.F., Lu, Z., Sircar, J., Kinefuchi, I., Bagnall, K.R., Salamon, T.R., Antao, D.S., Barabadi, B., and Wang, E.N. (2020). High heat flux evaporation of low surface tension liquids from nanoporous membranes. ACS Appl. Mater. Interfaces *12*, 7232–7238. https://doi.org/10.1021/acsami.9b20520.
4. Subramanian, N., Qamar, A., Alsaadi, A., Gallo, A., Ridwan, M.G., Lee, J.-G., Pillai, S., Arunachalam, S., Anjum, D., Sharipov, F., et al. (2019). Evaluating the potential of superhydrophobic nanoporous alumina membranes for direct contact membrane distillation. J. Colloid Interface Sci. *533*, 723–732. https://doi.org/10.1016/j.jcis.2018.08.054.
5. Xia, Y., Hou, Q., Jubaer, H., Li, Y., Kang, Y., Yuan, S., Liu, H., Woo, M.W., Zhang, L., Gao, L., et al. (2019). Spatially isolating salt crystallisation from water evaporation for continuous solar steam generation and salt harvesting. Energy Environ. Sci. *12*, 1840–1847. https://doi.org/10.1039/c9ee00692c.
6. Gao, Y., Li, D., Ru, J., Yang, M., Lu, L., Lu, L., Wu, J., Huang, Z., Xie, Y., and Gao, N. (2021). A numerical study on capillary-evaporation behavior of porous wick in electronic cigarettes. Sci. Rep. *11*, 10348. https://doi.org/10.1038/s41598-021-89685-4.
7. Lee, J., and Karnik, R. (2010). Desalination of water by vapor-phase transport through hydrophobic nanopores. J. Appl. Phys. *108*, 044315. https://doi.org/10.1063/1.3419751.
8. Xiao, R., Maroo, S.C., and Wang, E.N. (2013). Negative pressures in nanoporous membranes for thin film evaporation. Appl. Phys. Lett. *102*, 123103. https://doi.org/10.1063/1.4798243.
9. Wang, Q., and Chen, R. (2018). Ultrahigh flux thin film boiling heat transfer through nanoporous membranes. Nano Lett. *18*, 3096–3103. https://doi.org/10.1021/acs.nanolett.8b00648.
10. Li, Y., Alibakhshi, M.A., Zhao, Y., and Duan, C. (2017). Exploring ultimate water capillary evaporation in nanoscale conduits. Nano Lett. *17*, 4813–4819. https://doi.org/10.1021/acs.nanolett.7b01620.
11. Lu, Z., Wilke, K.L., Preston, D.J., Kinefuchi, I., Chang-Davidson, E., and Wang, E.N. (2017). An ultrathin nanoporous membrane evaporator. Nano Lett. *17*, 6217–6220. https://doi.org/10.1021/acs.nanolett.7b02889.
12. Li, Y., Chen, H., Xiao, S., Alibakhshi, M.A., Lo, C.-W., Lu, M.-C., and Duan, C. (2019). Ultrafast diameter-dependent water evaporation from nanopores. ACS Nano *13*, 3363–3372. https://doi.org/10.1021/acsnano.8b09258.
13. Lee, C., Wei, X., Kysar, J.W., and Hone, J. (2008). Measurement of the elastic properties and intrinsic strength of monolayer graphene. Science *321*, 385–388. https://doi.org/10.1126/science.1157996.
14. Buchheim, J., Schlichting, K.-P., Wyss, R.M., and Park, H.G. (2019). Assessing the thickness–permeation paradigm in nanoporous membranes. ACS Nano *13*, 134–142. https://doi.org/10.1021/acsnano.8b04875.
15. Feng, S., and Xu, Z. (2019). Edges facilitate water evaporation through nanoporous graphene. Nanotechnology *30*, 165401. https://doi.org/10.1088/1361-6528/aafcbd.
16. Fan, J., Wu, H., and Wang, F. (2020). Evaporation-driven liquid flow through nanochannels. Phys. Fluids *32*, 012001.
17. Boutilier, M.S.H., Sun, C., O'Hern, S.C., Au, H., Hadjiconstantinou, N.G., and Karnik, R. (2014). Implications of permeation through intrinsic defects in graphene on the design of defect-tolerant membranes for gas separation. ACS Nano *8*, 841–849. https://doi.org/10.1021/nn405537u.
18. Koenig, S.P., Wang, L., Pellegrino, J., and Bunch, J.S. (2012). Selective molecular sieving through porous graphene. Nat. Nanotechnol. *7*, 728–732. https://doi.org/10.1038/nnano.2012.162.
19. Huang, S., Dakhchoune, M., Luo, W., Oveisi, E., He, G., Rezaei, M., Zhao, J., Alexander, D.T.L., Züttel, A., Strano, M.S., and Agrawal, K.V. (2018). Single-layer graphene membranes by crack-free transfer for gas mixture separation. Nat. Commun. *9*, 2632. https://doi.org/10.1038/s41467-018-04904-3.
20. Surwade, S.P., Smirnov, S.N., Vlassiouk, I.V., Unocic, R.R., Veith, G.M., Dai, S., and Mahurin, S.M. (2015). Water desalination using nanoporous single-layer graphene. Nat. Nanotechnol. *10*, 459–464. https://doi.org/10.1038/nnano.2015.37.
21. Kidambi, P.R., Jang, D., Idrobo, J., Boutilier, M.S.H., Wang, L., Kong, J., and Karnik, R. (2017). Nanoporous atomically thin graphene membranes for desalting and dialysis applications. Adv. Mater. *29*, 1700277. https://doi.org/10.1002/adma.201700277.
22. Celebi, K., Buchheim, J., Wyss, R.M., Droudian, A., Gasser, P., Shorubalko, I., Kye, J.-I., Lee, C., and Park, H.G. (2014). Ultimate permeation across atomically thin porous graphene. Science *344*, 289–292. https://doi.org/10.1126/science.1249097.
23. Xie, Q., Xiao, S., and Duan, C. (2017). Geometry-dependent drying in dead-end nanochannels. Langmuir *33*, 8395–8403. https://doi.org/10.1021/acs.langmuir.7b02027.
24. Nair, R.R., Wu, H.A., Jayaram, P.N., Grigorieva, I.V., and Geim, A.K. (2012). Unimpeded permeation of water through helium-leak–tight graphene-based membranes. Science *335*, 442–444. https://doi.org/10.1126/science.1211694.
25. Wang, L., Boutilier, M.S.H., Kidambi, P.R., Jang, D., Hadjiconstantinou, N.G., and Karnik, R. (2017). Fundamental transport mechanisms, fabrication and potential applications of nanoporous atomically thin membranes. Nat. Nanotechnol. *12*, 509–522. https://doi.org/10.1038/nnano.2017.72.
26. Phan, V.N., Nguyen, N.-T., Yang, C., Joseph, P., Djeghlaf, L., Bourrier, D., and Gue, A.-M. (2010). Capillary filling in closed end nanochannels. Langmuir *26*, 13251–13255. https://doi.org/10.1021/la1010902.
27. Washburn, E.W. (1921). The dynamics of capillary flow. Phys. Rev. *17*, 273–283. https://doi.org/10.1103/physrev.17.273.
28. Eijkel, J.C.T., Dan, B., Reemeijer, H.W., Hermes, D.C., Bomer, J.G., and van den Berg, A. (2005). Strongly accelerated and humidity-independent drying of nanochannels induced by sharp corners. Phys. Rev. Lett. *95*, 256107. https://doi.org/10.1103/physrevlett.95.256107.
29. Eames, I.W., Marr, N.J., and Sabir, H. (1997). The evaporation coefficient of water: a review. Int. J. Heat Mass. Transf. *40*, 2963–2973. https://doi.org/10.1016/s0017-9310(96)00339-0.
30. Persad, A.H., and Ward, C.A. (2016). Expressions for the evaporation and

condensation coefficients in the hertz-knudsen relation. Chem. Rev. *116*, 7727–7767. https://doi.org/10.1021/acs.chemrev.5b00511.

31. Raj, R., Maroo, S.C., and Wang, E.N. (2013). Wettability of graphene. Nano Lett. *13*, 1509–1515. https://doi.org/10.1021/nl304647t.

32. Thomas, J.A., and McGaughey, A.J.H. (2008). Reassessing fast water transport through carbon nanotubes. Nano Lett. *8*, 2788–2793. https://doi.org/10.1021/nl8013617.

33. Tunuguntla, R.H., Henley, R.Y., Yao, Y.-C., Pham, T.A., Wanunu, M., and Noy, A. (2017). Enhanced water permeability and tunable ion selectivity in subnanometer carbon nanotube porins. Science *357*, 792–796. https://doi.org/10.1126/science.aan2438.

34. Dreyer, D.R., Park, S., Bielawski, C.W., and Ruoff, R.S. (2010). The chemistry of graphene oxide. Chem. Soc. Rev. *39*, 228–240. https://doi.org/10.1039/b917103g.

35. Kuan, A.T., Lu, B., Xie, P., Szalay, T., and Golovchenko, J.A. (2015). Electrical pulse fabrication of graphene nanopores in electrolyte solution. Appl. Phys. Lett. *106*, 203109. https://doi.org/10.1063/1.4921620.

36. Rollings, R.C., Kuan, A.T., and Golovchenko, J.A. (2016). Ion selectivity of graphene nanopores. Nat. Commun. *7*, 11408. https://doi.org/10.1038/ncomms11408.

37. Shan, Y.P., Tiwari, P.B., Krishnakumar, P., Vlassiouk, I., Li, W.Z., Wang, X.W., Darici, Y., Lindsay, S.M., Wang, H.D., Smirnov, S., and He, J. (2013). Surface modification of graphene nanopores for protein translocation. Nanotechnology *24*, 495102. https://doi.org/10.1088/0957-4484/24/49/495102.

38. Cohen-Tanugi, D., and Grossman, J.C. (2012). Water desalination across nanoporous graphene. Nano Lett. *12*, 3602–3608. https://doi.org/10.1021/nl3012853.

39. Schoch, R.B., Han, J., and Renaud, P. (2008). Transport phenomena in nanofluidics. Rev. Mod. Phys. *80*, 839–883. https://doi.org/10.1103/revmodphys.80.839.

40. Rizzuto, A.M., Cheng, E.S., Lam, R.K., and Saykally, R.J. (2017). Surprising effects of hydrochloric acid on the water evaporation coefficient observed by Raman thermometry. J. Phys. Chem. C *121*, 4420–4425. https://doi.org/10.1021/acs.jpcc.6b12851.

41. Stein, D., Kruithof, M., and Dekker, C. (2004). Surface-charge-governed ion transport in nanofluidic channels. Phys. Rev. Lett. *93*, 035901. https://doi.org/10.1103/physrevlett.93.035901.

42. Lee, C., Joly, L., Siria, A., Biance, A.-L., Fulcrand, R., and Bocquet, L. (2012). Large apparent electric size of solid-state nanopores due to spatially extended surface conduction. Nano Lett. *12*, 4037–4044. https://doi.org/10.1021/nl301412b.

43. Labuntsov, D.A., and Kryukov, A.P. (1979). Analysis of intensive evaporation and condensation. Int. J. Heat Mass. Transf. *22*, 989–1002. https://doi.org/10.1016/0017-9310(79)90172-8.

44. Ghasemi, H., and Ward, C.A. (2011). Mechanism of sessile water droplet evaporation: kapitza resistance at the solid–liquid interface. J. Phys. Chem. C *115*, 21311–21319. https://doi.org/10.1021/jp207293f.

45. Lu, Z., Kinefuchi, I., Wilke, K.L., Vaartstra, G., and Wang, E.N. (2019). A unified relationship for evaporation kinetics at low Mach numbers. Nat. Commun. *10*, 2368. https://doi.org/10.1038/s41467-019-10209-w.